Volume-selective magnetic resonance imaging using an adjustable, single-sided, portable sensor

Jeffrey L. Paulsen[a], Louis S. Bouchard[b], Dominic Graziani[a], Bernhard Blümich[c], and Alexander Pines[a,1]

[a]College of Chemistry, University of California, Berkeley, CA 94720; [b]Department of Chemistry and Biochemistry, University of California, 607 Charles E. Young Drive East, Los Angeles, CA 90095; and [c]Institute of Technical and Macromolecular Chemistry, RWTH Aachen University, D-52056 Aachen, Germany

Contributed by Alexander Pines, November 5, 2008 (sent for review October 1, 2008)

Portable, single-sided NMR sensors can operate under conditions inaccessible to conventional NMR while featuring lower cost, portability, and the ability to analyze arbitrary-sized objects. Such sensors can nondestructively probe the interior of samples by collecting images and measuring relaxation and diffusion constants, and, given careful shimming schemes, even perform chemical analysis. The inherently strong magnetic-field gradients of single-sided sensors developed so far has prevented imaging of materials with high water content, such as biological tissues, over large volumes whereas designs with more homogeneous fields suffer from low field strength and typically cannot probe volumes larger than ≈10 cm^3. We present a design with a continuously adjustable sensitive volume, enabling the effective volume to be enlarged several fold. This capability allows for imaging in reasonable times of much bigger objects and opens the door to the possibility of clinical imaging with portable sensors. We demonstrate MRI in axial and sagittal planes, at different depths of the sensitive volume and T_1-weighted contrast in a tissue sample.

adjustable magnet | ex situ NMR | mobile NMR | single-sided NMR | permanent magnet

Nuclear magnetic resonance (NMR) and magnetic resonance imaging (MRI) can provide noninvasive chemical analysis and imaging by using the endogenous contrast of materials, regardless of optical opacity. NMR can ascertain physical parameters such as diffusion, flow, and structure of porous materials and biological tissue, and can probe length scales from nanometers to meters. Clinical MRI is usually performed at high magnetic fields for an improved signal-to-noise ratio (SNR) and associated image resolution, but it requires bulky, expensive, immobile, and often hazardous magnets. Low-field NMR, however, has emerged as an attractive option for imaging in the field and in the presence of metal (1), and it provides more versatile contrast for relaxation weighted images (2). Because these smaller sensors typically operate in geometric environments where the static field is weak and inhomogeneous, the development of single-sided sensors has necessitated the development of novel methodologies and pulse sequences (3–13) designed to minimize image distortions and improve our ability to perform traditional chemical-shift spectroscopy (14). Therefore, objects can be nondestructively probed and one may obtain relaxation, diffusion, or image data over relatively small regions and obtain chemical-shift spectra with careful magnet shimming schemes (15). In spite of these advances, only relatively small volumes can be imaged (10 cm^3 or less) or analyzed spectroscopically (20 mm^3 or less).

Mobile NMR sensors can vary in 2 aspects that have a fundamental impact on their performance: (*i*) the orientation of the field relative to the surface of the sensor and (*ii*) the type of sensitive region that the magnet produces (homogeneous field over a volume vs. thin slices in a strong gradient). The first case dictates the type of radio frequency (RF) excitation and detection coil that can be used. A field that is perpendicular to the sensor, for instance, requires an RF field parallel to the surface of the magnet and a figure-eight coil instead of a single loop that results in much lower SNR efficiencies for both excitation and detection. In the second case, the sensitive region can be optimized for higher static magnetic fields at the expense of field homogeneity, which provides better sensitivity per unit volume but results in very small usable volumes and substantial signal losses to diffusion (which are a consequence of strong magnetic-field gradients). Another option is to generate more homogeneous fields, which results in larger sensitive volumes and less diffusional losses but at the expense of field strength. These trade-offs are empirical findings that arise during magnet design processes and appear to be of a fundamental nature.

Sensors with strong gradients in the static field typically use the gradient select slice positions by retuning of the resonant RF circuit. Diffusion attenuation for large gradient devices is a serious impediment to SNR, requiring rapid pulsing to compensate for the effect*. The pulse rate is limited by coil ringing and the amount of power that can be delivered to the RF coil, thus these devices do not normally allow measurements of samples with high water content. The NMR MOUSE (4) features a 5-kG field in a ≈0.1-cm^3 volume near its surface, whereas the NMR MOLE (9) design has a 767-G field over a 6.2-cm^3 volume located 5 cm above its surface. Because of the lower diffusion attenuation in homogeneous field sensors, they are better suited for studying liquid samples such as aqueous solutions and biological tissue (9). The current homogeneous field sensors are of fixed configurations and can sample only a single useful region in space, which is typically <10 cm^3 in size.

We present here the development and implementation of a device with an adjustable sensitive volume, with the use of a continuously adjustable array of permanent magnets that can be mechanically tuned in a manner similar to the tuning of guitar strings. Thus, we are able to perform MRI of liquid samples over volumes that are much larger than a conventional portable magnet†. Our magnetic-field orientation and RF field configuration are optimized for low power requirements and high sensitivity‡. The design follows a recently-developed inverse magnet design method (17) that is adapted to a cylindrical geometry that leads naturally to the feature of adjustability. In terms of the above discussion on optimal geometry, we have opted for an intermediate field strength (≈600–700 G) so that

Author contributions: J.L.P., L.S.B., D.G., B.B., and A.P. designed research; J.L.P. and D.G. performed research; J.L.P. and D.G. analyzed data; and J.L.P., L.S.B., D.G., B.B., and A.P. wrote the paper.

The authors declare no conflict of interest.

[1]To whom correspondence should be addressed. E-mail: pines@berkeley.edu.

*The free induction signal decays caused by diffusion according to $\exp[-(1/3)\gamma^2G^2Dt^3]$ from a uniform gradient (16), where G is the gradient and D is the self-diffusion coefficient. For a 1 kG/cm gradient, the signal from water decays by half in 2 ms, whereas in a 10 G/cm gradient, this decay time scale is 50 ms.

†Although a fixed field sensor could be scaled to sample larger volumes, it would have to be designed to produce a distant sensitive volume, but the magnetic field strength of a distant volume is inherently weak.

‡Adjustability also provides a way to compensate for the variability across different permanent magnet blocks and imperfections within each block that inevitably arise during the manufacturing process.

© 2008 by The National Academy of Sciences of the USA

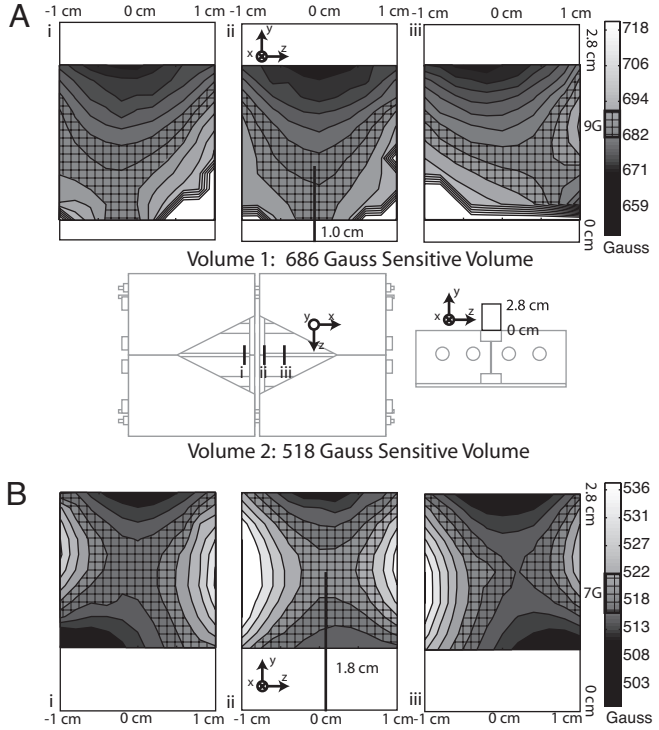

Fig. 1. Contour field maps of sensitive volume 1 (686 G) (*A*) and volume 2 (518 G) (*B*) for 3 slices above the magnet. The homogeneous region of each covers a different region of space. As the sensitive volume is pushed further out, its shape changes into a saddle point. The field strengths for each slice are based on the proton resonance frequency of a 2-mm-diameter, 2-mm-long piece of rubber positioned over an 11 × 11 grid spanning 2 × 2 cm. The center shows a drawing of the magnet surface to identify positions i, ii, and iii.

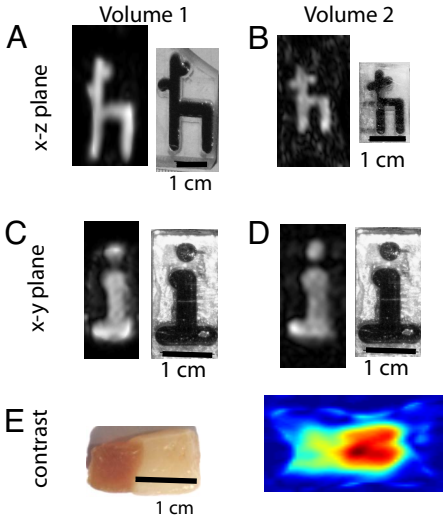

Fig. 2. MR images collected by the sensor of water phantoms and of a pork belly sample using two of its sensitive volumes. (A–*D*) MR images of the symbols ''ℏ'' (*A* and *B*) and ''i'' (*C* and *D*) carved into a polycarbonate block and filled with 2 mM Gd-DPTA solutions. Photographs of the phantoms filled with dyed water are shown next to the MR images. All samples are 10 mm thick. Within the sensitive region the phantom's shapes are accurately reproduced. Images in A and C were acquired in volume 1, and images in *B* and *D* were acquired in volume 2. The true image resolution (field of view divided by acquisition matrix) was 2 mm (*A* and *B*) and 1 mm (*C* and *D*). (*E*) An *x-z* plane MR image of a piece of pork belly at 2-mm resolution showing T_1-weighted contrast between fat and muscle. All images were Gaussian-filtered and adjusted according to a sensitivity map. The acquisition matrices were 17 × 17 (*A* and *E*), 25 × 25 (*B*), and 13 × 29 (*C* and *D*), and images were reconstructed by zero-filling to 51 × 51 (*A* and *E*), 75 × 75 (*B*), and 39 × 87 (*C* and *D*).

a larger, but homogeneous, volume could be excited by using a vertical RF field. This compromise has the advantage of large volumes, better RF sensitivity, and less diffusion attenuation.

Results

The sensor consists of an array of 4 cylindrical permanent magnet rods with a prescribed orientation of the magnetization for each rod, and this set of orientations depends on the location and size of the desired sensitive volume. Flat RF and gradient coils placed near the surface of the magnet are used for imaging. The details of the sensor design, assembly, and characterization are provided in *Materials and Methods*. A volume size and position is chosen for the experiment, and a computer program calculates the magnet rod orientations that are then adjusted. To illustrate adjustability and imaging functionalities of the sensor, we picked 2 nonoverlapping sensitive volumes centered at a distance 1.0 and 1.8 cm from the magnet surface (or equivalently, 3.0 and 3.8 cm from the center of the magnet rods). We note that the magnet array can also produce sensitive volumes over a continuous range of distances (17). Each of these volumes was characterized by acquiring a magnetic field map as shown in Fig. 1, which verifies that the volumes are sufficiently homogeneous for RF excitation by using a typical resonant circuit. The first sensitive volume (volume 1) produces a (686 ± 6) G field over a 8.9-cm^3 region (Fig. 1*A*), and the more distant sensitive volume (volume 2) produces a (518 ± 6) G field >8.1 cm^3 (Fig. 1*B*). As the sensitive volume is pushed away from the sensor's surface, it shrinks along the direction of the magnet rod axes because homogeneity along this axis relies on the extent to which these rods approximate rods of infinite length; this approximation breaks down at distances on the order of a quarter of the rod length (17).

MR images along axial and sagittal planes for both sensitive volumes are shown in Fig. 2. The first set of 2D images (Fig. 2 *A–D*) are of phantoms consisting of gadopentetate dimeglumine (Gd-DPTA)-doped water in polycarbonate frames and demonstrate the sensor's ability to image in orthogonal planes and the ability to obtain images of high water content samples, which is not possible with sensors that feature a large gradient. The doping was used to increase the water relaxation rates to resemble parameters typical of water in tissue. All of these MR images accurately depict the shape of the phantoms with reasonable in-plane spatial resolutions, as seen by the comparison with photographs of the phantoms shown in Fig. 2. Fig. 2 *A*, *C*, and *D* shows MR images obtained with extended acquisition times (34 min and 1 h 37 min, respectively). Fig. 2*B* illustrates the result with a much shorter (10 min) acquisition time, which still yields acceptable performance.

To demonstrate MRI of biological tissues, a T_1-weighted image of a pork belly sample is shown in Fig. 2*E*. In Fig. 2*E* the fat and muscle tissues are clearly differentiated as red and yellow/green regions, respectively, within the chosen color map. In this case, the imaging sequence uses a shortened repetition delay to create so-called T_1-weighted contrast between muscle and fat.

Conclusions

We have developed a MRI sensor with an adjustable sensitive volume that can be moved away from the sensor's surface, thereby enlarging the effective volume that can be probed with a single-sided, portable sensor. It allows for significantly larger effective imaging volumes than otherwise possible with a fixed sensor of the same size. At each given depth, it can produce a

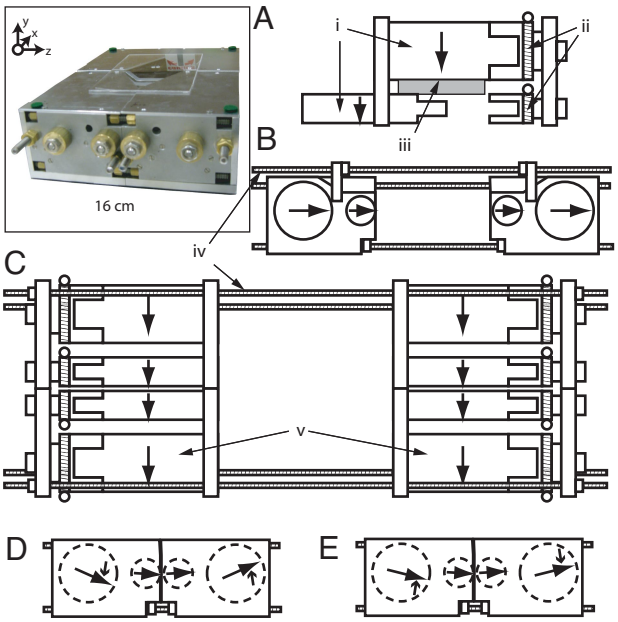

Fig. 3. The magnet and a schematic of its assembly. (*A*) Individual magnet rods (*i*) are placed into the frame's 4 sections by hand. (*B*) These sections are brought together into halves, where a system of threaded rods and nuts (*iv*) opposes the attractive forces between the sections and allows them to come together gradually in the correct orientation. (*C*) A system of threaded rods and nuts (*iv*) brings together the 2 halves, holding them in place against the repulsion between the 2 halves. (*D*) Rods are rotated to their calculated optimal values (24.1° and 3.5° for the outer and inner rods, respectively). These orientations are then adjusted several times according to a coarse field map of the target volume. (*E*) To push the sensitive volume further out, the outer rods are turned 7.5° into the plane containing the rods. (*i*) The $Nd_2Fe_{14}B$ cylindrical magnet rods are all 9 cm long and flatted for 1 cm on one of the ends to allow the frame to hold them in the desired orientations. The arrows indicate the orientation of the magnetization. The small and large rods have 2- and 4-cm diameters, respectively. (*ii*) At the flattened end of each magnet rod, a gear and worm drive assembly controls the rod's orientation. (*iii*) A temporary 1-cm-thick board keeps the appropriate distance between the magnet rods while they are placed into each of the frame's sections. (*iv*) A system of threaded rods and nuts bring the magnet's sections together in a controlled manner. (*v*) In the final configuration each rod is paired with another to create a rod that is effectively 18 cm long.

≈10-cm^3 homogeneous volume with residual gradients small enough that biological tissues can be imaged without significant diffusion losses. Although the imaging times and spatial resolution (5 min and 2 mm for Fig. 2*E*) are quite reasonable in its current configuration, further improvements in acquisition efficiency are still possible with the use of subsampling techniques (18) and multiple coil techniques (19, 20). These latter techniques are particularly advantageous with a pure phase encoding MRI scheme as used here. Although much larger gains in SNR are also possible with the use of prepolarization (21), hyperpolarization (22, 23), microcoil (24), and remote detection (25) techniques, the sensor can already achieve reasonable imaging performance in its current configuration.

Methods

Magnet Design, Assembly, and Characterization. The sensor was designed by an inverse technique we developed based on a least-squares fit of optimal dipole magnitudes to produce a desired target field (17). For arrays of parallel permanent magnet rods, it yields optimal rod radii and orientations of the magnetization given a desired target field and rod locations. The rod positions were determined by a global search, where our inverse technique determines the optimal dipole strengths and orientations for each of a representative set of possible arrangements and the search picks the best array. To determine how the rod orientations should vary to move the sensor's sensitive volumes,

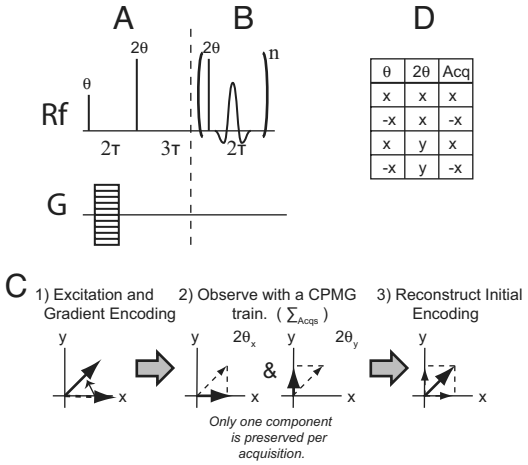

Fig. 4. The MRI pulse sequence for imaging in inhomogeneous fields consists of a 2D pure phase encoding step followed by a CPMG train for signal averaging. (*A*) An initial RF pulse, gradient pulse, and echo excite and spatially encode the spins. (*B*) A final echo train acquires the signal. (*C*) The overall effect of the echo train in an inhomogeneous field is to retain only the component along the axis of the refocusing pulse. (*D*) Thus, the relative phases of the pulses and acquisition are cycled between runs to obtain both components of the encoded phase. This phase cycle also eliminates any residual ringing from the refocusing pulse.

the method uses constraints to optimize rod orientations given fixed magnet rod sizes. See ref. 17 for details.

The magnet's implementation for our sensor consists of 4 pairs of cylindrical $Nd_2Fe_{14}B$ magnet rods (*i* and *v* in Fig. 3) magnetized perpendicularly to their axes with $\mu_o M = 1.35$ T and held in place mechanically by an aluminum and bronze frame (Fig. 3) containing a few small stainless-steel components for reinforcement. Each magnet rod pair consists of 2 collinear cylindrical magnet rods separated by a small gap that allows for improved magnetic field homogeneity along the direction of the rod axes (26). The magnet rods at the far ends are flattened so to be gripped by a brace that connects the rod to its own axle. This axle is fixed to the frame so to allow free rotation and attached to it is a gear and wormdrive assembly to control the rod's orientation by turning a key and a brake to fix its orientation once in position.

The frame consists of 4 boxes held together by a system of nuts and threaded rods, and each box contains 2 of the magnet rods (Fig. 3). This division exists to provide a straightforward procedure to bring the magnet rods into position (Fig. 3). The rod orientations for volume 1 corresponds to the original optimization in ref. 17, whereas volume 2 corresponds to a sensitive volume located an additional 1 cm away from the surface. All final rod orientations may need to be adjusted from their calculated values because the rods' magnetizations will vary on the order of several percent from their ideal values. A coarse field map of the target volume is obtained, and fine-tuning is performed as needed. Detailed field maps following this fine adjustment are shown in Fig. 1, where we measured the proton resonance frequency 2-mm rubber sample at each position of an 11 × 11 grid spanning 2 cm × 2 cm in the *yz* plane for each of 5 slices spaced 1 cm apart along the *x* axis, 3 of which are shown in Fig. 1. This fine-tuning only needs to be done once after the magnet is assembled for the first time.

Gradients. Single-sided gradient coils for spatial encoding along each axis were designed by using a least-squares target field method that minimizes the stored energy, allowing for higher slew rates. Each coil was printed as 4 copies in a spiral pattern on a single, 4-layered, printed circuit board to maximize the gradient field strength per unit current. The coils produce a gradient field of 0.7, 1.1, and 0.7 G $cm^{-1}A^{-1}$ for the *x*, *y*, and *z* gradient coils, respectively, with slew rates of 37, 64, and 49 G·cm^{-1}·ms^{-1}. The gradients were placed above the sample opposite the RF coil for volume 1, whereas the gradients were right on top of the magnet with the RF coil raised above by 1 cm for volume 2.

Imaging. All images were collected with an Apollo LF Spectrometer (Tecmag), an AE Techron LVC 2016 Linear amplifier, and a CPC MRI Plus RF amplifier. The imaging pulse sequence (Fig. 4) is a basic pure phase-encoding imaging sequence with a Carr–Purcell–Meiboom–Gill (CPMG) acquisition train and is from ref. 27. The sequence was implemented with a 8-μs nominal $\pi/2$ pulse

length, 100–200 810-μs acquisition echoes, a 700-μs gradient pulse length, and 200- and 75-ms recycle delays for the Gd-DPTA-doped water and pork belly samples, respectively. Sensitivity maps were collected with the same conditions as the images to be corrected by using uniform phantoms that spanned most of the field of view. Image intensities were adjusted according to sensitivity maps by dividing the object image intensities by those of the sensitivity map with a soft threshold applied to regions below a certain sensitivity. The water phantom and pork belly samples uniformly spanned 1 and 0.5 cm, respectively, across the nonimaged axis. A pure 2D phase encoding was used for spatial localization (6). It has the advantage of reducing the effects of magnetic field inhomogeneities to an overall scaling factor across the image and leaving the image free of inhomogeneity artifacts. At low magnetic fields, multiple acquisitions are generally required to provide enough signal averaging, so pure phase encoding does not cost additional scan time. The sequence begins with an initial RF excitation pulse followed by a gradient pulse for phase encoding (Fig. 4*A*) and a CPMG train for signal averaging. For the CPMG train, we change the phase of the refocusing pulse by $\pi/2$ between the acquisitions (Fig. 4*C*), taking advantage of the fact that the sequence will effectively keep only the component of each spin initially along the axis of the refocusing pulse (Fig. 4*D*) as explained in refs. 28 and 29.

ACKNOWLEDGMENTS. We thank David Hoult for stimulating discussions, Vasiliki Demas for help with the initial setup of the spectrometer and RF circuitry, and Sasa Antonijevic for assistance with assembling the magnet. This work was supported by the Director, Office of Science, Office of Basic Energy Sciences, Materials Sciences and Engineering Division, of the U.S. Department of Energy under Contract DE-AC02-05CH11231. B.B.'s work in Berkeley was supported by the Miller Institute for Basic Research in Science.

1. Moessle M, *et al.* (2006) SQUID-detected microtesla MRI in the presence of metal. *J Magn Reson* 179:146–151.
2. Lee S-K, *et al.* (2005) Squid-detected MRI at 132 μT with T_1-weighted contrast established at 10 μT-300 mT. *Magn Reson Med* 53:9–14.
3. Murphy DP (1995) Advances in MWD and formation evaluation for 1995. *World Oil* 216:39–49.
4. Eidmann G, Savelsberg R, Blümler P, Blümich B (1996) The NMR MOUSE, a mobile universal surface explorer. *J Magn Reson* 122:104–109.
5. Fukushima E, Jackson J (1999) Unilateral magnets: An idea and some history. *NMR News Lett* 490:40–42.
6. Casanova F, Blümich B (2003) Two-dimensional imaging with a single-sided NMR probe. *J Magn Reson* 163:38–45.
7. Marble AE, Mastikhin IV, Colitts BG, Balcom BJ (2005) An analytical methodology for magnetic field control in unilateral NMR. *J Magn Reson* 174:78–87.
8. McDonald PJ, Aptaker PS, Mitchell J, Mulheron M (2007) A unilateral NMR magnet for substructure analysis in the built environment: The surface garfield. *J Magn Reson* 185:1–11.
9. Manz B, *et al.* (2006) A mobile one-sided NMR sensor with a homogeneous magnetic field: The NMR MOLE. *J Magn Reson* 183:25–31.
10. Kleinberg RL (1996) Well logging. *Encyclopedia NMR* 105:2960–4969.
11. Meriles CA, Sakellariou D, Heise H, Moulé AJ, Pines A (2001) Approach to high-resolution ex situ NMR spectroscopy. *Science* 293:82–85.
12. Topgaard D, Martin RW, Sakellariou D, Meriles CA, Pines A (2004) Shim pulses for NMR spectroscopy and imaging. *Proc Natl Acad Sci USA* 101:17576–17581.
13. Perlo J, Casanova F, Blümich B (2006) Single-sided sensor for high-resolution NMR spectroscopy. *J Magn Reson* 180:274–279.
14. Blümich B, Perlo J, Casanova F (2008) Mobile single-sided NMR. *Progr Nucl Magn Reson Spectr* 52:197–269.
15. Perlo J, Casanova F, Blümich B (2007) Ex situ NMR in highly homogeneous fields: ^{1}H spectroscopy. *Science* 315:1110–1112.
16. Callaghan PT (1991) *Principles of Nuclear Magnetic Resonance Microscopy* (Oxford Univ Press, Oxford).
17. Paulsen JL, Frank J, Demas V, Bouchard LS (2008) Least-squares magnetic-field optimization for portable NMR magnet design. *IEEE Trans Magnet* 44, 10.1109/tmag.2008.2001697.
18. Lustig M, Donoho DL, Santos JM, Pauly JM (2008) Compressed sensing MRI. *IEEE Signal Process Mag* 25:72–82.
19. Pruessmann KP, Weigner M, Scheidegger MB, Boesiger P (1999) SENSE: Sensitivity encoding for fast MRI. *Magn Reson Med* 42:952–962.
20. Giovannetti G, *et al.* (2008) Low field elliptical MR coil array designed by FDTD. *Concepts Magn Reson B* 33:32–38.
21. Matter NI, *et al.* (2006) Three-dimensional prepolarized magnetic resonance imaging using rapid acquisition with relaxation enhancement. *Magn Reson Med* 56:1085–1095.
22. Oros AM, Shah NJ (2004) Hyperpolarized xenon in NMR and MRI. *Phys Med Biol* 49:R105–R153.
23. McCarney ER, Armstrong BD, Lingwood MD, Han S (2007) Hyperpolarized water as an authentic magnetic resonance imaging contrast agent. *Proc Natl Acad Sci USA* 104:1754–1759.
24. Sakellariou D, Le Goff G, Jacquinot J-F (2007) High-resolution, high-sensitivity NMR of nanolitre anisotropic samples by coil spinning. *Nature* 447:694–697.
25. Moulé AJ, *et al.* (2003) Amplification of xenon NMR and MRI by remote detection. *Proc Natl Acad Sci USA* 100:9122–9127.
26. Anferova S, *et al.* (2007) Improved Halbach sensor for NMR scanning of drill cores. *Magn Reson Imag* 25:474–480.
27. Perlo J, Casanova F, Blümich B (2004) 3D imaging with a single-sided sensor: An open tomograph. *J Magn Reson* 166:228–235.
28. Ahola S, Perlo J, Casanova F, Stapf S, Blümich B (2006) Multiecho sequence for velocity imaging in inhomogeneous rf fields. *J Magn Reson* 182:143–151.
29. Hürlimann MD, Griffin DD (1999) Spin dynamics of Carr-Purcell-Meiboom-Gill sequences in grossly inhomogeneous B_0 and B_1 fields and application to NMR well logging. *J Magn Reson* 143:120–135.